Quantum teleportation of light beams

T. C. Zhang, K. W. Goh, C. W. Chou, P. Lodahl, and H. J. Kimble
Norman Bridge Laboratory of Physics 12-33, California Institute of Technology, Pasadena, CA 91125
(Dated: July 11, 2002)

We experimentally demonstrate quantum teleportation for continuous variables using squeezed-state entanglement. The teleportation fidelity for a real experimental system is calculated explicitly, including relevant imperfection factors such as propagation losses, detection inefficiencies and phase fluctuations. The inferred fidelity for input coherent states is $F = 0.61 \pm 0.02$, which when corrected for the efficiency of detection by the output observer, gives a fidelity of 0.62. By contrast, the projected result based on the independently measured entanglement and efficiencies is 0.69. The teleportation protocol is explained in detail, including a discussion of discrepancy between experiment and theory, as well as of the limitations of the current apparatus.

I. INTRODUCTION

The *No Cloning Theorem* prohibits making an exact copy of an unknown quantum state [1]. Yet, it is nevertheless possible to transport an unknown quantum state from one place to another without having the associated physical object propagate through the intervening space by way of a process termed *quantum teleportation* in the landmark work by Bennett et al. [2] in 1993. This "disembodied" transport of quantum states is made possible by utilizing shared quantum entanglement and classical communication between the sending and receiving locations. In recent years, quantum teleportation has played a central role in quantum information science and has become an essential tool in diverse quantum algorithms and protocols [3, 4].

By contrast, progress on an experimental front has been rather more modest in the actual attainment of quantum teleportation [5, 6, 7, 8]. An overview of these various experiments as well as operational criteria for gauging laboratory success can be found in Refs. [9, 10]. Significantly, to date only the experiment of Furusawa et al. [7] on continuous variables has achieved unconditional quantum teleportation [11].

The purpose of this paper is to present a report of our progress in the continuation of the experiment as reported by Furusawa et al. [7] and as described in Ref. [12]. We give a detailed description of our quantum teleportation apparatus and procedures, and include recent experimental results [13]. Some notable distinctions between our current experiment and the previous one by Furusawa et al. are improved EPR entanglement, better detection efficiencies, and ultimately, a higher fidelity between the input and teleported output states. We also investigate in some detail the various factors that limit the quality of the teleportation procedure under realistic conditions and as are applicable to the experimental setup. We provide a detailed model of the entire experiment that includes essentially all of the dominant loss mechanisms and utilize this model to gain insight into the limitations of the current apparatus and protocols, and thereby to discover methods of circumventing these limitations.

Our experiment is based on the continuous variable teleportation protocol first proposed in [14], which in turn was motivated by the work of Vaidman [15]. In our realization of this protocol, an entangled EPR state [16] is created from two independent squeezed fields. One half of this entangled state (called EPR1) is sent to Alice, who in turn combines it at a 50/50 beamsplitter with an unknown input state that is intended for teleportation. Note that the input quantum state is unknown to both Alice and Bob. Alice subsequently measures the x and p quadratures of the two output fields from the beamsplitter, the x quadrature for one beam and the p quadrature for the other. This measurement of (x, p) provides the continuous variable analogy to a Bell-state measurement for the discrete variable case [17]. In the limit of perfect EPR correlations, Alice gains no information about the input state. The output photocurrents from Alice's two quadrature measurements are transmitted to Bob via classical information channels. Bob then uses them to perform a continuous phase space displacement on the second EPR beam (EPR2), thereby generating the teleported output state. For perfect EPR correlations, the teleported state has unit fidelity with the original unknown input state, as can be verified by "Victor" who both generates the original input and measures the teleported output. Of course, the limit of this ideal case is unattainable in any laboratory setting. This necessitates the introduction of operational criteria to gauge the success of the protocol, as discussed in Refs. [9, 10], and as will be applied in relation to our experiment.

The paper is organized as follows. In Sec. II we discuss the fidelity for quantum teleportation in the presence of losses and phase fluctuations, including importantly for the EPR beams. In Sec. III this model is connected to the laboratory via a detailed discussion of the generation of our EPR resource, including specifications of the optical parametric oscillator (OPO) parameters, the obtainable squeezing, and the characterization of the EPR state. The technical details of the actual implementation of the quantum teleportation protocol are discussed in depth in Sec. IV with emphasis on the phase-lock servo systems and the calibration of the classical information channels. Here, we also present new data on the teleportation of coherent states of light. These experimental

data are compared to theoretical calculations based on the relevant parameters for the experiment, with each parameter measured in absolute terms without adjustment. Finally, we collect our conclusions in Sec. V, together with an outlook for future progress.

II. THEORY

In this section a theoretical description of the quantum teleportation protocol for continuous variables is given. This is a generalization of previous work in order to include all relevant detector inefficiencies and phase offsets for the experiment. The discussion is divided into two parts: in Sec. II A the effect of nonideal homodyne detectors is investigated while Sec. II B concerns phase fluctuations due to imperfect phase-lock servos. Both effects turn out to be of substantial importance in trying to accurately model experimental data.

A. Detection inefficiencies

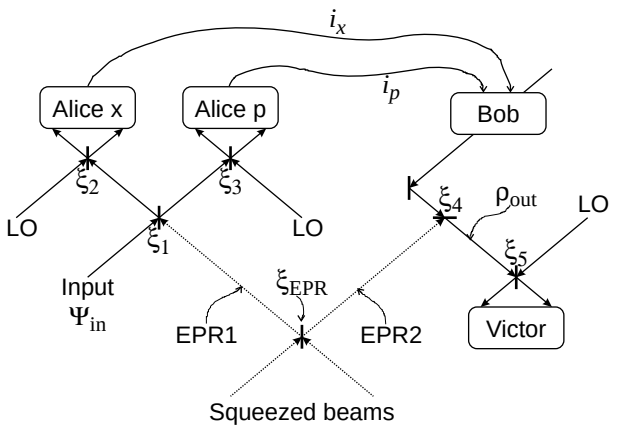

FIG. 1: Main parts in the teleportation protocol for continuous variables. Indicated are the relevant efficiencies $(\xi_{1\to5}, \xi_{EPR})$ that limit the teleportation fidelity.

Fig. 1 shows a simplified schematic of the experiment for teleportation of an unknown quantum state provided by the verifier Victor and characterized by a pure input state $|\psi_{in}\rangle$. The process is as follows: Alice performs measurements of the two quadratures x and p of the fields obtained by combining the unknown input state with EPR1. This is done by implementing two balanced homodyne detectors where the signal fields are each combined with a strong coherent local oscillator (LO) and the resulting output intensities are measured. Subtracting the two photocurrents from a given set of detectors results in a signal proportional to the quadrature amplitude, with the relevant quadrature selected by the phase of the LO. The efficiency of the homodyne detectors can be characterized by the visibilities (ξ_2, ξ_3) of the overlap between the LOs and the output beams from Alice's beamsplitter, as well as the detectors' quantum efficiency (α). Furthermore, the visibility (ξ_1) of the overlap between the input state and EPR1 is relevant.

Because of the nature of the EPR correlations, the effect of Alice's quadrature measurements is to project EPR2 onto a state that differs from the unknown input state only by a phase space displacement. The necessary displacement, however, depends on the outcome of Alice's measurements. Hence the task for Bob is to perform this phase space displacement with the classical information received from Alice by way of the photocurrents (i_x, i_p) shown in Fig. 1. In practice this is accomplished by overlapping EPR2 with a phase and amplitude modulated coherent state on a 99/1 beamsplitter. This modulation is directly driven (with suitable gain and phase compensation) by the photocurrents (i_x, i_p) from Alice's detectors. The relevant efficiency is the visibility (ξ_4) between EPR2 and the modulated coherent state. Finally, the quality of the teleportation can be checked by a third party (Victor) that performs homodyne detection on the output state. The visibility of Victor's homodyne detector is denoted ξ_5.

As discussed in more detail in Refs. [9, 10], the performance of the teleportation protocol can be quantified by the fidelity F, which is defined by

$$F = \langle \psi_{in} | \rho_{out} | \psi_{in} \rangle , \tag{1}$$

which is simply the overlap between the input state $|\psi_{in}\rangle$ (which is assumed to be a pure state) and the output state characterized by a density matrix ρ_{out}. In the limit of perfect detectors (unity efficiencies) but with a finite degree of EPR correlation, the fidelity for quantum teleportation of coherent states can be shown to be [7, 9]

$$F = \frac{2}{\sigma_Q} \exp\left[-\frac{2}{\sigma_Q} |\beta_{out} - \beta_{in}|^2 \right] , \tag{2}$$

where

$$\sigma_Q = \sqrt{(1+\sigma_W^x)(1+\sigma_W^p)}, \tag{3a}$$

$$\sigma_W^x = \sigma_W^p = g^2 + \frac{1}{2} e^{2r_+}(1-g)^2 + \frac{1}{2} e^{-2r_-}(1+g)^2. \tag{3b}$$

Here σ_W^x and σ_W^p are the variances (in the Wigner representation) of the teleported x and p quadratures that emerge from Bob's beamsplitter (as shown in Fig. 1 at ρ_{out}). g is gain of the classical channels, where we have assumed that the two classical channels have the same gain and that any phase offsets have been appropriately compensated. Furthermore, β_{in}, β_{out} are the amplitudes of the unknown input field and teleported output field respectively. Finally, r_+, r_- are the anti-squeezing and squeezing parameters, respectively, for the two equally squeezed beams used to produce the EPR correlations, as will be discussed in detail in Sec. III C.

Any real experiment of course suffers from finite losses in propagation and detection, with the individual efficiencies being critical due to the fragility of quantum states of light. It turns out that the general expression (2) for the fidelity still applies to the case with losses, but the variances of the quadratures of the teleported field generalized. In addition, we take into account the fact that we do not observe the output state directly, but instead measure the output photocurrent from Victor's balanced homodyne detector. If we assume as before that the input states to Alice are coherent states, then the quadrature variance σ_V^x recorded by Victor for the teleported output state can be written as

$$\sigma_V^x = 1 - r_B^2\xi_4^2\xi_5^2\eta_V^2 - g_x^2\xi_1^2 + \frac{2g_x^2}{\xi_2^2\eta_{Ax}^2} + \frac{e^{-2r_-}}{2}\left(g_x\xi_1 + r_B\xi_4\xi_5\eta_V\right)^2 + \frac{e^{2r_+}}{2}\left(g_x\xi_1 - r_B\xi_4\xi_5\eta_V\right)^2, \tag{4}$$

and the variance for the p quadrature is given by $\sigma_V^p = \sigma_V^x\left(g_x \to g_p, \eta_{Ax} \to \eta_{Ap}, \xi_2 \to \xi_3\right)$. The fidelity is then obtained by replacing $\sigma_W^{x,p}$ with $\sigma_V^{x,p}$ in Eqs. (3). The nonunit reflectivity of Bob's beamsplitter appears as a loss factor r_B, where in our experiment, $|r_B|^2 = 0.99$. η_i are detector efficiency factors directly related to the quantum efficiencies α_i by $\alpha_i = \eta_i^2$, where the subscripts denote Alice x, Alice p or Victor. $g_{x,p}$ are the suitably normalized gains for the x and p classical channels through which Alice sends information to Bob.

In terms of the model given in Fig. 1, the gains $g_{x,p}$ are given explicitly by

$$g_x = \frac{g_{x,(0)}}{\sqrt{2}} t_B\xi_2\xi_5\eta_{Ax}\eta_V, \tag{5a}$$

$$g_p = \frac{g_{p,(0)}}{\sqrt{2}} t_B\xi_3\xi_5\eta_{Ap}\eta_V. \tag{5b}$$

Here, $g_{x,(0)}$ and $g_{p,(0)}$ are dimensionless gains that account for the translation of the photocurrents $i_{x,p}$ into fields by Bob's amplitude and phase modulation, where the point of reference is immediately before his beamsplitter, which is taken to have amplitude reflection and transmission coefficients (r_B, t_B). Note that the formal limit of a phase-space displacement by Bob is achieved only for the case $(t_B \to 0, g_{x,(0)} \to \infty)$, with the product $t_B g_{x,(0)}$ held constant.

The convention that we adopt for the normalization of the gains $g_{x,p}$ in Eqs. (4) and (5) is such that $g_x = g_p = 1$ results in $\beta_V = \beta_{in}$, and hence reflects an optimal reconstruction of the input state for any sensible values of the squeezing parameters $r_\pm$. The caveat here is that since we measure Victor's photocurrent and not the field emerging from Bob, we effectively set $|\beta_V|^2 = |\beta_{in}|^2$ and not $|\beta_{out}|^2 = |\beta_{in}|^2$ as required by the protocol, where it can be easily shown that

$$|\beta_V|^2 = \xi_5^2\eta_V^2\,|\beta_{out}|^2. \tag{6}$$

This defect in our measurement will be discussed quantitatively when we present our experimental data in Sec. IV D. Note that if Victor has perfect detection efficiency ($\xi_5 = \eta_V = 1$), the problem vanishes, and the result given in Eq. (4) is exact for the teleported output field emerging from Bob's beamsplitter.

The corresponding variances obtained by Alice's homodyne detectors are given by

$$\sigma_A^x = 1 + \frac{1}{4}\left(e^{-2r_-} + e^{2r_+} - 2\right)\xi_1^2\xi_2^2\eta_{Ax}^2, \tag{7a}$$

$$\sigma_A^p = 1 + \frac{1}{4}\left(e^{-2r_-} + e^{2r_+} - 2\right)\xi_1^2\xi_3^2\eta_{Ap}^2. \tag{7b}$$

Several limiting cases associated with these expressions are worth noting. In the classical case where there is no EPR entanglement ($r_+ = r_- = 0$), and with perfect homodyne detectors ($\xi_{1\to5} = \eta_i = 1$), we obtain $\sigma_V^x = \sigma_V^p = 3$, corresponding to three units of vacuum noise in Victor's homodyne detector. One unit stems from the vacuum noise intrinsic to the input coherent state, while the two extra units can be traced back as the quantum duties added in each crossing of the border between quantum and classical domains corresponding to Alice's quadrature measurements and Bob's phase space displacement [14]. This means that for classical teleportation of coherent states, the best achievement possible is reconstructing the input state with two extra units of vacuum noise added [9, 10]. The three vacuum units correspond to excess noise recorded in Victor's homodyne detector of 4.77 dB above the vacuum-state limit for his detector. With quantum entanglement it is possible to beat this limit and observe noise reduction below the 4.77 dB level in Victor's detector. The measured noise reduction can then be transferred into a fidelity through Eq. (2). As analyzed in Refs. [9, 10], the classical boundary for teleportation of coherent states is $F = 0.5$.

In the case of nonideal detectors, $g_x = g_p = 1$ still preserves optimal teleportation for the normalized gains, in the sense that $\beta_V = \beta_{in}$. However, the normalization is performed by effectively tuning the unnormalized gains $g_{(0)}$ by

$$g_{x,(0)}^{nonideal} \longrightarrow \left(\xi_2\xi_5\eta_{Ax}\eta_V\right)^{-1} g_{x,(0)}^{ideal}, \tag{8}$$

and similarly for p. Thus in the nonideal case, the actual gain is larger than in the ideal case, reflecting the fact that the gain must now compensate for Alice's and Victor's detection losses in order to ensure $\beta_V = \beta_{in}$. As a consequence, the fidelity drops below $F = 0.50$ with no entanglement ($r_\pm = 0$). In our experiment, the detection efficiencies are characterized by the measured visibilities and quantum efficiencies, which in the best case are given by $\xi_1 = 0.986$, $\xi_2 = \xi_3 = 0.995$, $\xi_4 = 0.988$, $\xi_5 = 0.985$, and $\alpha_V = \alpha_{Ax} = \alpha_{Ap} = 0.988$. With these experimentally achievable efficiency factors, we find that $\sigma_V^{x,p} = 4.84$ dB and $F = 0.494$ when $r_\pm = 0$.

Fig. 2 shows the excess noise recorded by Victor and Alice x (or equivalently Alice p) as a function of the amount of squeezing, both for the ideal case with perfect detection efficiencies, and for the nonideal case with

detector efficiencies given above. With no squeezing in the ideal case, we see from the solid curves that Victor obtains exactly 4.77 dB of excess noise as expected and as discussed above while Alice is shot-noise-limited. With imperfect detection efficiencies as shown by the dashed curves, Alice remains shot-noise-limited, while Victor records excess noise higher than 4.77 dB. In fact, the only relevant efficiencies that drive Victor's recorded noise above 4.77 dB involve Alice's homodyne detectors, namely (ξ_2, η_{Ax}) for the x quadrature, and (ξ_3, η_{Ap}) for the p quadrature. All other detection losses can be compensated by the gains $g_{x,p}$ when $r_\pm = 0$.

As the squeezing is increased so that now $r_\pm > 0$, Victor records noise reduction below the $r_\pm = 0$ level. By contrast, Alice's noise increases above the vacuum level at her detectors, and in the limit of infinite squeezing, Alice's noise diverges while Victor's excess noise is suppressed to the vacuum level. Notice that with perfect detection efficiencies, $\sigma_V^{x,p} < 4.77$ dB for any $r_\pm > 0$. With imperfect efficiencies, this is not true. In effect, some of the squeezing is "wasted" to compensate for the nonideal efficiencies. Since our experimental visibilities are close to unity, this loss can be neglected as it is below the level of other experimental uncertainties for small values of $r_\pm$. However, with large degrees of squeezing, the disparity between the ideal and nonideal cases increases and cannot be ignored, as can be seen from Fig. 2. The reason for this trend is that now the visibilities ξ_1 and ξ_4 that characterize the overlap of the EPR beams with Alice's and Bob's relevant beams, as well as the non-unit reflectivity r_B of Bob's beamsplitter, become important. The losses from non-unit ξ_1 and ξ_4 obviously cannot be compensated by the gains of the classical channels.

The noise reduction at Victor can be transferred into a teleportation fidelity, with the result plotted in Fig. 3. The solid and dashed curves for the ideal and nonideal cases mimic the conclusions discussed above for the variances $\sigma_V^{x,p}$ measured by Victor.

Of course, the teleportation fidelity is very dependent on the detector efficiencies. We investigate this point in more detail in Fig. 4, where the fidelity is plotted as a function of a single global visibility ξ (assuming $\xi_{1\to5} = \xi$) and where the quantum efficiencies of all the photodetectors are $\alpha = 0.988$. This figure clearly illustrates the need for a high amount of squeezing as well as very efficient spatial mode-matching of our optical beams to achieve high fidelity quantum teleportation.

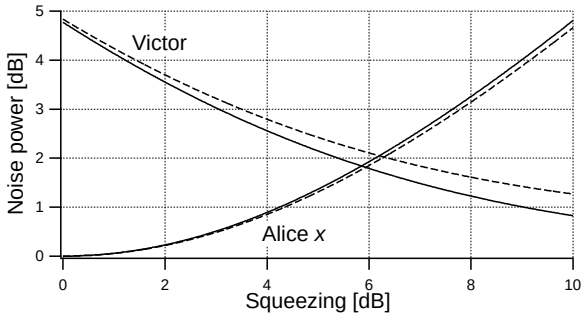

FIG. 2: Noise powers in dB above the vacuum-state limit for Alice's x detector and for Victor's detector as a function of the degree of squeezing of each squeezed vacuum state constituting the EPR state. The solid traces are for an ideal case where both Alice and Victor have perfect detection efficiency and all relevant beams are perfectly overlapped, that is, $\xi_{1\to5} = \alpha_i = 1$. The dashed traces show the noise levels for a real (nonideal) case where the visibilities correspond to the experiment described below and are $\xi_1 = 0.986$, $\xi_2 = \xi_3 = 0.995$, $\xi_4 = 0.988$, $\xi_5 = 0.985$, and the quantum efficiencies of photodetectors are $\alpha_i = 0.988$. The squeezing given in the figure is the squeezing just before the EPR beamsplitter.

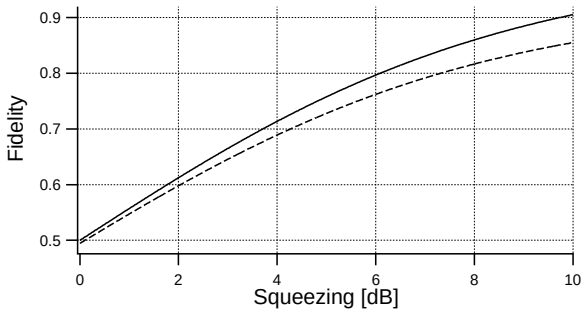

FIG. 3: The fidelity for Victor's teleported output as a function of the degree of squeezing with same parameters as in Fig. 2. Again, the solid trace describes a perfect case with ideal detectors, while the dashed trace describes the imperfect case as relevant to our experiment.

B. Phase fluctuations

Not only losses associated with the detection efficiencies limit the achieved fidelity for quantum teleportation. Also the quality of the servo-control systems that lock various phases (e.g., the local oscillator phases at Alice's detectors) appear to be of significant importance, since phase deviations due to nonideal locking turn out to deteriorate the noise reduction measured by Victor. We will see that this mathematically corresponds to mixing in terms proportional to the anti-squeezed quadratures of the squeezed beams constituting the EPR state.

In a realistic model of the experiment we include phase offsets of four servo locks: the EPR lock, Alice's two homodyne detectors, as well as Bob's lock of the phase between the second EPR field and the classical field. The analysis presented here will be a straightforward generalization of the derivation in [18] based on the Heisenberg picture. The quadratures of the two EPR fields (1 and 2) are obtained by combining two squeezed fields with the angle between the squeezing ellipses equal to $\pi/2$. Although we have investigated a more complete model, here we account for the phase deviation away from $\pi/2$ by introducing an angle offset θ_E for field 2. In this sim-

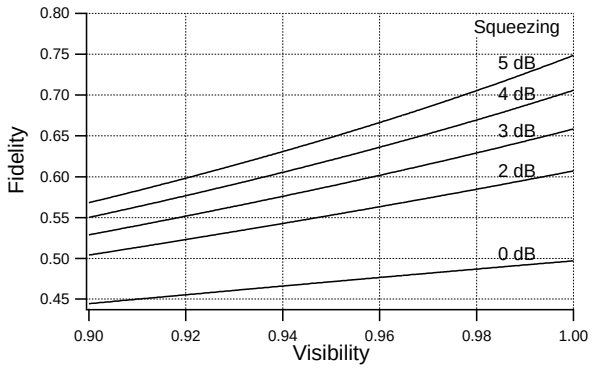

FIG. 4: Fidelity as a function of visibility for different values of the degree of squeezing. We have assumed $\xi_{1\to 5} = \xi$ and $\alpha = 0.988$.

ple nonideal case, we obtain for the fields emerging from the EPR beamsplitter

$$\hat{x}_{1,2} = \frac{1}{\sqrt{2}}\left(e^{r_+}\hat{x}_1^{(0)} \mp \cos\theta_E e^{-r_-}\hat{x}_2^{(0)} \mp \sin\theta_E e^{r_+}\hat{p}_2^{(0)}\right), \tag{9a}$$

$$\hat{p}_{1,2} = \frac{1}{\sqrt{2}}\left(e^{-r_-}\hat{p}_1^{(0)} \mp \cos\theta_E e^{r_+}\hat{p}_2^{(0)} \pm \sin\theta_E e^{-r_-}\hat{x}_2^{(0)}\right), \tag{9b}$$

where $\hat{x}_{1,2}^{(0)}$ and $\hat{p}_{1,2}^{(0)}$ are vacuum state operators for (x,p) for the input beams 1 and 2 to the beamsplitter, respectively. Further downstream, EPR beam 1 is mixed with the unknown input state on a 50/50 beamsplitter creating the modes $\hat{u} = (\hat{a}_{in} - \hat{a}_1)/\sqrt{2}$ and $\hat{v} = (\hat{a}_{in} + \hat{a}_1)/\sqrt{2}$, and Alice measures the two quadrature amplitudes of the corresponding state in her homodyne detectors. Allowing for small phase deviations θ_{Ax} and θ_{Ap} in the detection process, we find that the quadratures measured by Alice now become

$$\hat{x}_u(\theta_{Ax}) = \hat{x}_u\cos\theta_{Ax} + \hat{p}_u\sin\theta_{Ax}, \tag{10a}$$

$$\hat{p}_v(\theta_{Ap}) = \hat{p}_v\cos\theta_{Ap} - \hat{x}_v\sin\theta_{Ap}. \tag{10b}$$

Finally, Bob performs a phase space displacement of the second EPR beam by overlapping with the coherent beam containing the classical information received from Alice. Allowing again for a phase offset θ_B in Bob's phase-space displacement, we calculate that the quadrature operators for the teleported state exiting the apparatus for investigation by Victor is given by

$$\hat{x}_V = \hat{x}_2\cos\theta_B + \hat{p}_2\sin\theta_B + \sqrt{2}\hat{x}_u(\theta_{Ax}), \tag{11a}$$

$$\hat{p}_V = \hat{p}_2\cos\theta_B - \hat{x}_2\sin\theta_B + \sqrt{2}\hat{p}_v(\theta_{Ap}), \tag{11b}$$

where the normalized gains of the classical channels have been taken to be unity. Using Eqs. (9) and (10), we arrive at expressions for the Heisenberg operators for the teleported field received by Victor, namely

$$\begin{aligned}\sqrt{2}\hat{x}_V =& \left(\cos\theta_B - \cos\theta_{Ax}\right)e^{r_+}\hat{x}_1^{(0)} + \left(\sin\theta_B - \sin\theta_{Ax}\right)e^{-r_-}\hat{p}_1^{(0)} \\ &+ \left[\cos\theta_E(\cos\theta_B + \cos\theta_{Ax}) - \sin\theta_E(\sin\theta_B + \sin\theta_{Ax})\right]e^{-r_-}\hat{x}_2^{(0)} \\ &+ \left[\sin\theta_E(\cos\theta_B + \cos\theta_{Ax}) + \cos\theta_E(\sin\theta_B + \sin\theta_{Ax})\right]e^{r_+}\hat{p}_2^{(0)} + \sqrt{2}\cos\theta_{Ax}\hat{x}_{in} + \sqrt{2}\sin\theta_{Ax}\hat{p}_{in},\end{aligned} \tag{12a}$$

$$\begin{aligned}\sqrt{2}\hat{p}_V =& -\left(\sin\theta_B + \sin\theta_{Ap}\right)e^{r_+}\hat{x}_1^{(0)} + \left(\cos\theta_B + \cos\theta_{Ap}\right)e^{-r_-}\hat{p}_1^{(0)} \\ &+ \left[\sin\theta_E(\cos\theta_{Ap} - \cos\theta_B) + \cos\theta_E(\sin\theta_{Ap} - \sin\theta_B)\right]e^{-r_-}\hat{x}_2^{(0)} \\ &+ \left[\sin\theta_E(\sin\theta_{Ap} - \sin\theta_B) + \cos\theta_E(\cos\theta_B - \cos\theta_{Ap})\right]e^{r_+}\hat{p}_2^{(0)} + \sqrt{2}\cos\theta_{Ap}\hat{p}_{in} - \sqrt{2}\sin\theta_{Ap}\hat{x}_{in}.\end{aligned} \tag{12b}$$

By utilizing these expressions, the variances of the two quadratures measured by Victor can be calculated. Assuming the phase excursions are small, we expand to lowest order. We recall that the aim of this calculation is to describe the impact of phase fluctuations in the various servo-controls. Hence we assume that there are no static offsets (which we believe our current procedures adequately null), so that all the phase excursions vanish on average, $\overline{\theta} = 0$, and only deviations expressed by the second order moments contribute. Furthermore, it is assumed that all the phase fluctuations are independent, so that products of phases vanish on average.

After some algebra, we finally arrive at

$$\sigma_V(x) = \left\langle \Delta\hat{x}_V^2 \right\rangle = 1 + \left[2 - \frac{1}{2}\overline{\theta_{Ax}^2} - \frac{1}{2}\overline{\theta_B^2} - 2\overline{\theta_E^2}\right] e^{-2r_-} + \left[\frac{1}{2}\overline{\theta_{Ax}^2} + \frac{1}{2}\overline{\theta_B^2} + 2\overline{\theta_E^2}\right] e^{2r_+}, \quad (13a)$$

$$\sigma_V(p) = \left\langle \Delta\hat{p}_V^2 \right\rangle = 1 + \left[2 - \frac{1}{2}\overline{\theta_{Ap}^2} - \frac{1}{2}\overline{\theta_B^2}\right] e^{-2r_-} + \left[\frac{1}{2}\overline{\theta_{Ap}^2} + \frac{1}{2}\overline{\theta_B^2}\right] e^{2r_+}, \quad (13b)$$

where the various $\overline{\theta_i^2}$ are meant to be associated with the residual RMS fluctuations arising from the nonideal performance of our locking servos. Explicit dependence on the phase θ_V of Victor's LO is given by

$$\sigma_V[x(\theta_V)] = \sigma_V(x)\cos^2\theta_V + \sigma_V(p)\sin^2\theta_V. \quad (14)$$

These equations make quantitative the obvious intuition that the effect of the phase fluctuations is to add extra noise in the quadratures measured by Victor through components proportional to the anti-squeezed quadrature. In fact, relatively small phase fluctuations ($\sim 1^\circ$ RMS) can degrade the noise reduction that would otherwise have been recorded by Victor, and consequently also the achieved fidelity.

From these equations, we see that particular phase fluctuations contribute in quite different ways. Phase fluctuations at Bob contribute equally to excess noise in the x and p quadratures and will consequently be seen as a constant shift in the noise measured in Victor's homodyne detector while scanning the local oscillator. The same effect is found from fluctuations in the locking of the local oscillator phases at Alice x and Alice p provided $\overline{\theta_{Ax}^2} = \overline{\theta_{Ap}^2}$. However, phase fluctuations in the EPR lock are seen to modify Victor's x and p quadratures differently and therefore imply modulation of the noise measured by Victor. The relevant second order moments $\overline{\theta_i^2}$ for the various locks can be obtained experimentally by measuring the RMS noise of the error signals in locked operation. Typically measurements give $\sqrt{\overline{\theta_i^2}} \simeq 2$ to 6 degrees. From Eqs. (13) it is seen that fluctuations in the phase with which the squeezed beams are combined to form the EPR beams are most critical since $\overline{\theta_E^2}$ contributes with a coefficient four times higher than the other phase terms to the mixing with the anti-squeezing term.

Fig. 5 shows the calculated noise in Victor's homodyne detector for different levels of phase fluctuations in the EPR lock employing realistic values of squeezing and anti-squeezing for the experiment discussed in the following sections. The modulation of Victor's signal is seen to be up to about 0.2 dB peak to peak which turns out to imply a significant reduction of the achieved fidelity.

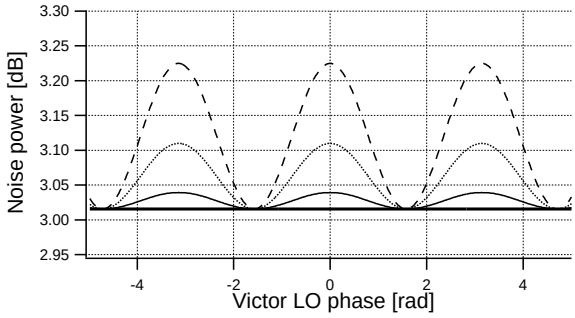

FIG. 5: Noise power recorded by Victor's balanced detector when scanning his local oscillator for $\sqrt{\overline{\theta_E^2}} = 0, 2, 4, 6$ degrees (corresponding to the bold, thin, dotted, and dashed curves, respectively), and for $\overline{\theta_{Ax}^2} = \overline{\theta_{Ap}^2} = \overline{\theta_B^2} = 0$. Realistic values of the degrees of squeezing (-3 dB) and of anti-squeezing (7 dB) have been used.

III. GENERATION OF THE QUANTUM RESOURCE

A more complete figure of the experimental setup is given in Fig. 6. A 10 W Verdi was used to pump a single frequency Ti:Sapphire laser operating at 866 nm. This laser system provided about 1.6 W of IR. About 80% to 85% of this light was sent to an external frequency doubler to generate an efficient 433 nm pump source for the optical parametric oscillator (OPO). Typically about 300 mW of blue light was produced that could be mode-matched to the OPO using a triangular ring cavity. Furthermore, the pump was divided into two beams, which allowed pumping the OPO from two directions to produce two independent squeezed beams. A detailed description of this setup for generation of highly squeezed light can be found in Ref. [19]. About 10% of the IR light from the Ti:Sapphire laser was spatially filtered in a mode cleaning cavity and used down stream in the experiment for locking the OPO, as local oscillators in the homodyne detectors, for Bob's displacement beam, and as the input coherent state for the actual teleportation. Combining the two squeezed beams on a 50/50 beamsplitter with the phases locked so that the squeezing ellipses are perpendicular to each other, the EPR state was generated which is the quantum resource necessary for the actual quantum teleportation protocol described previously in relation to Fig. 1. In the current section a detailed description of the generation of the EPR state is given with a careful characterization of both classical and quantum properties of the OPO. The actual implementation of the full teleportation protocol follows in Sec. IV.

A. Loss and gain in the OPO

The OPO cavity was a bow-tie ring configuration consisting of two curved mirrors (radius of curvature 5 cm)

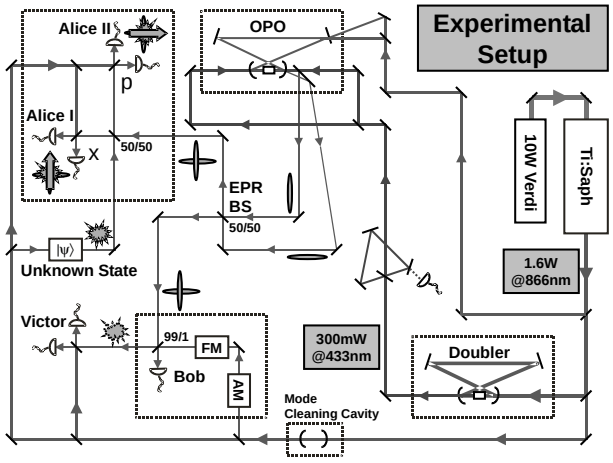

FIG. 6: Sketch illustrating the basic optical parts in the quantum teleportation experiment. See the main text for a careful discussion.

and two plane mirrors. The total cavity length was 48cm. The focus positioned between the two curved mirrors had a waist size of 21μm where the 1cm long nonlinear potassium niobate ($KNbO_3$) crystal was positioned. The use of a-cut potassium niobate allowed noncritical temperature phase-matching of a degenerate parametric process. To generate a pump for the OPO, the output from the Ti:Sapphire laser was frequency doubled in another external cavity also using potassium niobate as the nonlinear medium [20]. In this way 300 mW of pump light at 433 nm was generated.

In the OPO nonlinear down-conversion transformed energy from the pump field at 433 nm into the parametric field at 866 nm. In the current application the OPO was only driven below oscillation threshold, where spontaneous parametric emission can produce a squeezed vacuum state. The parametric field was resonant in the OPO while the pump light from the frequency doubler was divided into two beams, each of which was used in single pass of the OPO crystal from a counter propagating direction.

The OPO performance can be characterized once specifying the output coupler intensity transmission T, the effective nonlinearity E_{NL}, and the intracavity round-trip loss $\mathcal{L}$. In the current experiment the output coupler transmission was fixed at $T = 10\%$ which was chosen to optimize squeezing. The total information about the nonlinear interaction can be captured in the single parameter E_{NL} that depends on the focusing, length of the crystal, phase-matching and crystal properties. It can operationally be defined as $E_{NL} = P_2/P_1^2$, where P_2 is the second harmonic power generated in single pass frequency doubling of a fundamental pump P_1. In the current setup we measured $E_{NL} = 0.021W^{-1}$.

Contributing to the intracavity loss are nonideal antireflection coatings of the potassium niobate as well as leakage from the three high-reflection coated cavity mirrors. This passive loss was measured to be $\mathcal{L}_p = 0.3\%$. Unfortunately potassium niobate also suffers from an inherent loss mechanism that adds to the passive losses [21, 22]. This nonlinear loss arises in the OPO in the presence of the blue pump beam and has been termed blue-light-induced infrared absorption (BLIIRA). It is believed to originate from impurities in the crystal and is found to vary substantially from crystal sample to sample. At a high pump level of the OPO, BLIIRA turns out to be the dominating loss mechanism and eventually becomes the limiting factor for the amount of squeezing obtained. The losses $\mathcal{L}_b$ due to BLIIRA could be monitored in the OPO by measuring the reflection dip of the injected pump beam while scanning the cavity around resonance. Typical measurements of the total intracavity loss ($\mathcal{L} = \mathcal{L}_p + \mathcal{L}_b$) are shown in Fig. 7 as a function of the blue pump power. In this case the OPO was only pumped along one direction. We observe that the total loss increases up to about 2% at the highest pump level of $P_2 = 155\,\mathrm{mW}$.

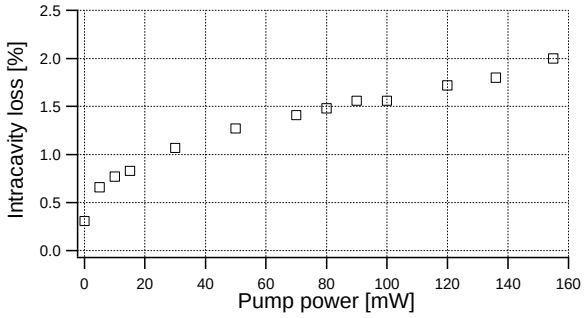

FIG. 7: Measured total intracavity round-trip cavity loss $\mathcal{L}$ as a function of the blue pump P_2. Note that the transmission T of the output coupler is not included.

The OPO could also be operated as a phase sensitive amplifier as a way to test the classical performance of the device. For that purpose an 866 nm beam was seeded into the OPO and by scanning the injection phase slowly, the amplification factor G was measured. When injecting the seed beam through the small transmission of a high reflection mirror and measuring the amplification of the light through the output coupler mirror, the gain is given by

$$G = \frac{1}{\left(1 - \sqrt{P_2/P_{2,t}}\right)^2}, \tag{15}$$

where $P_{2,t}$ is the oscillation threshold of the OPO given by

$$P_{2,t} = \frac{(T + \mathcal{L})^2}{4E_{NL}}. \tag{16}$$

Fig. 8 shows measured values of the gain as a function of pump power for single-sided pump of the OPO as well

as the theoretical curve based on the measured loss and nonlinearity. The gain diverges as approaching threshold and from these data we estimate $P_t \simeq 190$ mW. The agreement between experiment and theory is apparently quite good, here with no adjustable parameters.

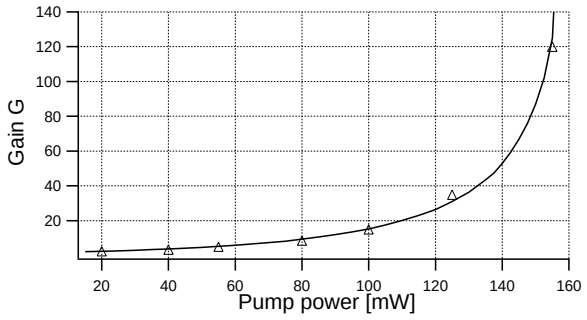

FIG. 8: Measured gain (points) and corresponding theoretical curve based on the measured loss and nonlinearity.

B. Squeezing

The phase-sensitive amplification in the OPO can be exploited for generating squeezed states of light. In this case the two input vacuum noise quadratures are amplified and deamplified, respectively, creating a squeezed vacuum state. Balanced homodyne detection allows phase sensitive detection of the quantum noise of the squeezed state. With this method the signal field is overlapped with a strong coherent local oscillator (LO) on a 50/50 beamsplitter. The two output beams from the beamsplitter are measured and the corresponding photocurrents subtracted. In this way the weak quantum noise of the signal is amplified to achieve a signal substantially above the thermal noise floor of the photodiodes. The photodiodes used were a special part made by Hamamatsu with a measured quantum efficiency $\alpha = 98.8 \pm 1.0\%$.

Two typical squeezing traces at different pump levels are presented in Fig. 9. They were obtained by recording Victor's noise power with the spectrum analyzer when scanning the phase of the LO. We observe the phase sensitive noise with the maximum and minimum corresponding to measuring the anti-squeezed and squeezed quadratures, respectively. With the signal beam blocked, the vacuum state level $\Phi_0^{(1)}$ was recorded, and squeezing corresponds to noise reduction below this level. By locking the LO phase to the squeezed quadrature, we obtained the flat traces below $\Phi_0^{(1)}$, as shown in Fig. 9. We infer squeezing of 3.73 dB below the vacuum level and anti-squeezing of 6.9 dB with pump power of 42 mW. At the higher pump level shown (107 mW), the degree of squeezing remained at 3.73 dB below the vacuum level while the degree of anti-squeezing increased to 10.8 dB.

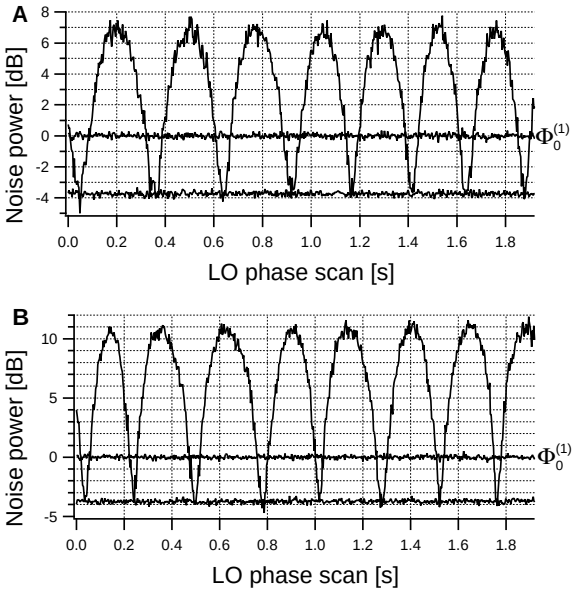

FIG. 9: Typical squeezing traces recorded by homodyne detection while scanning the phase of the LO. The measurement frequency was 1.475 MHz within a resolution bandwidth of 30 kHz and with a video bandwidth of 300 Hz. The flat traces at 0 dB are the respective vacuum levels $\Phi_0^{(1)}$, taken with a 5 trace average. Also displayed are the flat traces that correspond to the minimum noise level attained, again with a 5 trace average. These traces were obtained by locking the LO phase to the squeezed quadrature and lead to estimates of the squeezing and anti-squeezing of: (A) -3.73 dB and 6.9 dB with 42 mW pump power; and (B) -3.73 dB and 10.8 dB with 107 mW pump power. In both cases, the OPO was pumped from a single direction. Victor's detection efficiency was characterized by a homodyne visibility $\xi = 0.972$ and photodiode quantum efficiency $\alpha = 0.988$.

In the actual teleportation experiment the fidelity is ultimately limited by the amount of squeezing available. However, as discussed in Section II B, in a non-perfect experiment the amount of anti-squeezing is also important. In that section, we concluded that fluctuations in the servo locks will degrade the fidelity with contributions from the anti-squeezed quadratures. For that reason it is important to find the optimum operation point of the OPO where the degree of squeezing is large, while at the same point, the anti-squeezing has not grown too large. Such a compromise is made necessary by the BLIIRA, which limits the degree of quantum noise reduction in a power-dependent fashion, while the noise from the anti-squeezed quadrature continues to grow.

Fig. 10 shows the variation of the measured squeezing and anti-squeezing with the OPO pump power as well as the corresponding theoretical curves based on the measured experimental parameters (loss and nonlinearity) discussed in the previous section. The data have been corrected for the thermal noise level of the detectors, which was 17 dB below the vacuum noise level for

an LO of 2 mW. The squeezing is seen to level off at about −3.5 dB already at a pump of 45 mW while the anti-squeezing increases with the pump. This indicates that in the teleportation experiment it would be most favorable to operate at this relatively weak pump level of the OPO and that decreased teleportation fidelity might be expected when increasing the pump further (e.g., due to mixing in of noise from the anti-squeezed quadrature from the imperfections in servo control discussed in Sec. II B).

We note that the measured squeezing is lower than predicted from the OPO parameters discussed above; indeed we predict about 4.7 dB squeezing at high pump level. This discrepancy might be due to offset fluctuations in the OPO lock as well as phase fluctuations between the local oscillator and the squeezed beam in the homodyne detector. In favor of such an explanation is the fact that the theory predicts the anti-squeezed quadrature better than the squeezing quadrature, and the broad maximum from the anti-squeezing (see Fig. 9) is expected to be much less sensitive to phase fluctuations than the narrow squeezing minimum.

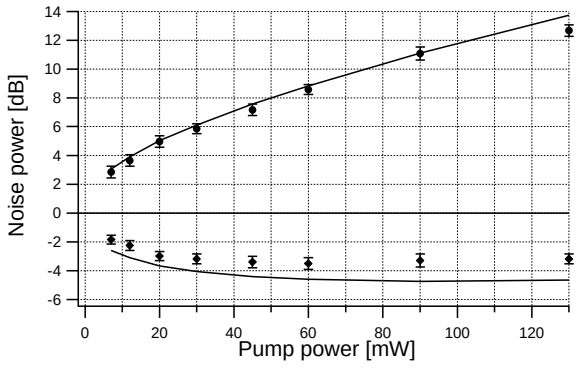

FIG. 10: Measured squeezing (diamonds) and anti-squeezing (dots) at a frequency offset of 1.475 MHz as a function of the OPO pump power when pumping from only one direction. The curves are the corresponding theoretical results for nonlinearity $E_{NL} = 0.019W^{-1}$ and measured cavity loss similar to that given in Fig. 7. The measured quantum efficiency was $\alpha = 0.988$, the homodyne visibility $\xi = 0.990$, and the propagation loss of the squeezed beam was 5.7%.

The above data were taken when the OPO was only pumped from a single direction. In order to obtain two squeezed beams necessary to generate the EPR correlations, the OPO was pumped in two counter-propagating directions. In this case we expect lower squeezing than from a single pumped OPO due to increased BLIIRA. This reduction in squeezing was measured to range from less than 0.3 dB at total pump powers below around 80 mW, to 0.5 dB at higher pump powers. To estimate the degree of squeezing in the double-pumped case, we take the degree of squeezing obtained in Fig. 9 and correct for Victor's homodyne visibility and finite detector thermal noise, to find that in the single-pumped case, we have −4.1 dB of available squeezing. Thus we estimate that we have about −3.6 to −3.8 dB squeezing in the double-pumped case.

C. EPR correlations

The EPR correlated beams were generated by combining two independently squeezed beams with the relative phase servo-locked to be $\pi/2$. These continuous variable EPR correlations are of the type originally discussed by Einstein, Podolsky, and Rosen [16]. The two output beams 1 and 2 from the EPR beamsplitter possess correlations as expressed by the variances $\sigma(x_1 \pm x_2) = 2\sigma_\pm$ and $\sigma(p_1 \pm p_2) = 2\sigma_\mp$, where σ_+ and σ_- are the variances of the anti-squeezed and squeezed quadratures of the two input beams, i.e. $\sigma_+ > 1$, $\sigma_- < 1$, and $\sigma_+\sigma_- \geq 1$. Without squeezing we obtain the vacuum noise level for two beams ($\Phi_0^{(2)}$) where $\sigma(x_1 \pm x_2) = \sigma(p_1 \pm p_2) = 2$. We observe that x_1 and x_2 are correlated while p_1 and p_2 are anti-correlated both to a level below the vacuum noise level. This is the same kind of quantum correlations first recorded for the light from a nondegenerate OPO [23, 24]. While noise reduction below the vacuum level is achieved when measuring correlations between the two EPR beams, the noise from only one of the EPR beams is phase independent and above the vacuum level. Indeed we find that $V(x_{1,2}) = V(p_{1,2}) = (\sigma_+ + \sigma_-)/2 \geq 1$, where unity is the vacuum level for a single beam ($\Phi_0^{(1)}$).

Experimentally the quality of the EPR state was investigated both by measuring one EPR beam as well as the correlations between the two beams. The noise in a single beam was measured while scanning the EPR phase θ_{EPR} between the two squeezed beams slowly compared to the scan rate of the local oscillator in the homodyne detector. An example is presented in Fig. 11. The rapid sweep of the local oscillator ensured that both quadratures were measured for each value of θ_{EPR} and gives rise to the fast variations in the trace. As explained above, the noise of a single EPR beam is expected to be phase independent and arises when overlapping the two squeezed beams with a mutual phase difference of $\theta_{EPR} = \pi/2$. Hence, this allows identification of this point in Fig. 11, and we observe excess noise in this case about 5 dB above the vacuum noise level. Furthermore, when the two squeezed beams are combined in phase ($\theta_{EPR} = 0$), two squeezed beams exit the beamsplitter giving noise reduction in this case roughly 3 dB below vacuum noise.

A direct measurement of the correlations between the two EPR beams was obtained via balanced homodyne detection of both EPR beams and subtracting the resulting photocurrents from the two sets of balanced detectors. In these measurements the EPR phase was locked at $\theta_{EPR} = \pi/2$ and one of the homodyne detectors was locked to measure a fixed quadrature. The trace in Fig. 12 was recorded by scanning the local oscillator θ_{LO} of the second homodyne detector, thus recording the variance $\sigma\left(x_1 - x_2(\theta_{LO})\right)$. Reduction below the vacuum

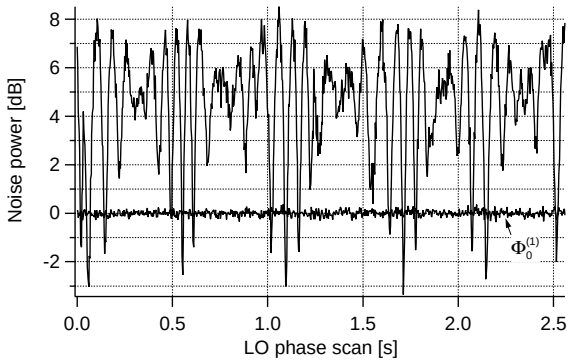

FIG. 11: Noise of one beam from the EPR beamsplitter as obtained by scanning the mutual phase difference between the two squeezed beams in addition to a rapid sweep (about 5 times faster) of the LO in the homodyne detector. The flat curve represents the vacuum state level for a single beam.

level for two beams ($\Phi_0^{(2)}$) was observed when the second homodyne detector measured the same quadrature as the first homodyne detector, i.e. for $\theta_{LO} = 0$. We observe correlations of the amplitude quadratures of about 2 dB with respect to the vacuum level. However, these data were taken in a non-optimized situation (e.g., inefficient OPO cavity alignment); the measured degree of squeezing at that time was under -3 dB. In the actual teleportation experiment inter-beam EPR correlations of more than 3 dB was obtained.

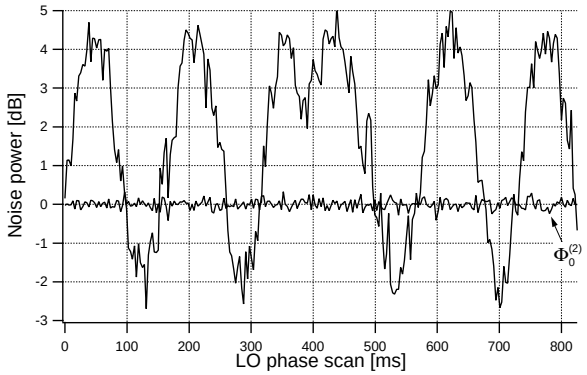

FIG. 12: Noise obtained by subtracting signals from two homodyne detectors measuring the two EPR beams while scanning one of the LO phases. The recorded quantity was $\sigma\left(x_1 - x_2(\theta_{LO})\right)$. The flat curve is the vacuum noise level for two beams.

IV. QUANTUM TELEPORTATION

Given the preceding description of how to generate the EPR state, we will now move on to discuss the complete quantum teleportation protocol. First the electronic servo locks implemented in the experiment are described, then the technique to calibrate the channels used by Alice to send classical information to Bob is presented. This establishes the basis for presenting the experimental results on quantum teleportation.

A. Phase locking

In the complete quantum teleportation experiment ten servo systems in total were implemented for locking optical phases and cavities. A summary of the locking techniques is given in Table I. Three of the servos (numbers $1-3$) are for locking cavities and use the standard Pound-Drever-Hall technique where reflection or transmission of RF modulation sidebands are used to derive an error signal. The frequency doubling cavity was locked by observing the cavity reflection dip off the input coupler, and generating an error signal using RF sidebands at 26 MHz. The OPO cavity was locked by observing a 1% pick-off from the transmitted light from a weak coherent beam injected through a high reflector. The injected signal carried 5 MHz sidebands for locking. Finally, the mode-cleaning cavity was locked in reflection using sidebands at 26 MHz.

The remaining seven servos were used to keep the optical phases properly aligned for successful teleportation [25]. Two weak injection beams were seeded into the two counterpropagating modes of the OPO and used for several purposes: to align the OPO cavity and the homodyne detectors, and to use for locking of optical phases. The two injected signals were phase modulated at 3 MHz (injection 1) and 5 MHz (injection 2) respectively, using an electro-optical modulator (EOM) in each signal path. The relative phase differences between the pump beams and the injected beams were locked using standard lock-in techniques where the error signal is derived from the phase sensitive amplification (due to the parametric gain in the OPO) of the injected signal. The phases are locked at maximum gain corresponding to the situation where the direction of the phasor of the coherent injected field is along the long axis of the squeezing ellipse of the squeezed vacuum beams.

The third phase-lock, the EPR phase lock, keeps the two independent squeezed beams incident on the EPR beamsplitter with a phase difference of $\pi/2$ to ensure the production of the EPR state. This was done by using 1% leakages from mirrors in the EPR beam paths. The DC interference signal between the two injected beams from the two distinct EPR paths was subtracted to produce an error signal centered around zero. This zero crossing corresponds to $\pi/2$ phase difference between the two squeezed beams.

To lock the local oscillators in Alice's two homodyne detectors, the RF beat notes between the LO and the 3 and 5 MHz sidebands on the injected beams were demodulated to produce the respective error signals for Alice I (3MHz) and II (5MHz). As the EPR phase lock described

NO.	BRIEF DESCRIPTION	LOCKING TECHNIQUE
1	Doubling cavity resonant to 866 nm	Pound-Drever-Hall via reflection, 26 MHz
2	OPO cavity resonant to 866 nm	Pound-Drever-Hall via transmission, 5 MHz
3	Mode cleaning cavity resonant to 866 nm	Pound-Drever-Hall via reflection, 26 MHz
4, 5	Relative phase between blue pump (433 nm) and injected beams 1 & 2 (866 nm) to zero (maximum gain)	Lock-in via 1% pick-off of cavity transmission
6	Relative phase between two squeezed beams to $\pi/2$ (to create EPR state)	DC interference fringe
7, 8	Alice's LOs to x and p quadratures	RF interference fringe, 3 MHz $\rightarrow x$, 5 MHz $\rightarrow p$
9	Bob's coherent beam to x quadrature	RF interference fringe, 3 MHz
10	Victor's LO to either x or p quadratures	RF interference fringe, 3 MHz $\rightarrow x$, 5 MHz $\rightarrow p$

TABLE I: Summary of the servo systems that were implemented. See main text for further discussion.

above already keeps the two injected beams at $\pi/2$ phase difference, the LOs in Alice I and II will also stay at $\pi/2$ relative phase difference. Bob's LO phase was locked using the RF interference fringe at 3 MHz between itself and the modulation sidebands transported with EPR2. This means that Alice I is locked to the same quadrature as Bob, which, by an arbitrary convention, sets Alice I as x and Alice II as p. Thus to complete the classical information channel, Alice I's measured output (photocurrent) was sent to Bob's amplitude modulator, and Alice II's output was sent to Bob's phase modulator. The teleported state then emerges from Bob's beamsplitter, and is sent to Victor for verification. Victor's LO phase can be either scanned, or locked to either 3 or 5 MHz to check x and p separately.

B. Classical information channels

A crucial part of the teleportation protocol is the transmission of classical information from Alice to Bob. In the present experiment the classical information is just the photocurrents from Alice's two homodyne detectors. These signals have to be faithfully transmitted to Bob without distortion and with proper phase and gain, and for that reason several RF amplifiers, filters and delay boxes were used in the classical channel paths. We typically measured Alice's and Victor's noise levels at 1.475 MHz, thus the electronics of the channels were optimized at that frequency. In the following we will present a method to perform the calibration of these classical channels.

To ensure that we are operating at a gain $g_x = g_p = 1$ such that $\beta_V = \beta_{in}$, we compared the photocurrents measured by Alice and Victor when there were no EPR beams present for the case of a coherent state of amplitude β_{in} sent to Alice as the input state. In practice, this was easily achieved by blocking the optical beam paths of the EPR state. In this case, it can be shown that when an amplitude or phase modulated beam is sent to Alice as the input state, the ratio between the spectral densities measured at Victor and Alice is given by

$$\frac{\Phi_V}{\Phi_A} = \frac{2}{\xi_2^2 \eta_A^2}, \tag{17}$$

where we have assumed Alice and Victor are measuring the same quadrature (either x or p), that $|\beta_{in}|^2 \gg 1$ and that the efficiencies are close to unity. We observe that Victor records a spectral density (i.e., noise power of the RMS photocurrent) two times (corresponding to 3 dB) higher than Alice x (or p). This factor of two can easily be understood since the input beam is split into two equal halves at Alice's 50/50 beamsplitter. Hence, this identifies a signature for the optimum condition of the classical gain.

On the other hand, for vacuum input, the ratio between Victor's and Alice's spectral densities, or equivalently, their variances since now $|\beta_{in}|^2 = 0$, is found to be

$$\frac{\sigma_V}{\sigma_A} = 1 + \frac{2}{\xi_2^2 \eta_A^2}, \tag{18}$$

when the classical gain is optimum. This means Victor's output is ≈ 3 times higher than Alice x (or p) again in the limit where all detector efficiencies are close to unity.

Fig. 13 shows the spectral density $\Phi_{Ax}(\Omega)$ of photocurrent fluctuations recorded at Alice x from input beams with modulation amplitudes corresponding to 24.9 dB and 0 dB (vacuum), respectively. The signal recorded at Alice p mirrors this trace, except that the coherent amplitude is shifted in phase by $\pi/2$, demonstrating that Alice x and p are $\pi/2$ apart in phase, as required. The corresponding traces for the spectral density $\Phi_V(\Omega)$ for Victor's detector are shown in Fig. 14. Here we show explicitly the $\pi/2$ phase shift when Victor's LO is phase-locked to the x and p quadratures, respectively. We see that Victor records 3 dB higher spectral density for the amplitude modulated input and 4.8 dB greater for the vacuum input, which indicates that the gain of the classical channels has been properly calibrated relative to the criteria of Eqs. (2) and (4).

We now turn our attention to the phases of the RF signals, keeping in mind the distinction between the phase

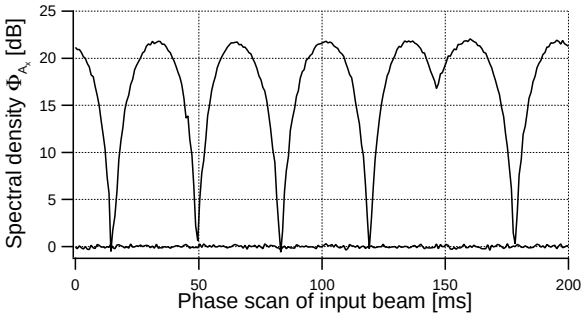

FIG. 13: Spectral density $\Phi_{Ax}(\Omega)$ relative to the vacuum level recorded by Alice x while scanning the phase of the input beam both for vacuum (flat trace), and an input beam with amplitude modulation at 24.9 dB above the vacuum noise level. The measured amplitude of this beam is 21.9 dB or 3 dB lower than the actual input, as explained in the text. The measurement frequency was 1.475 MHz, RBW 30 kHz, and VBW 1 kHz.

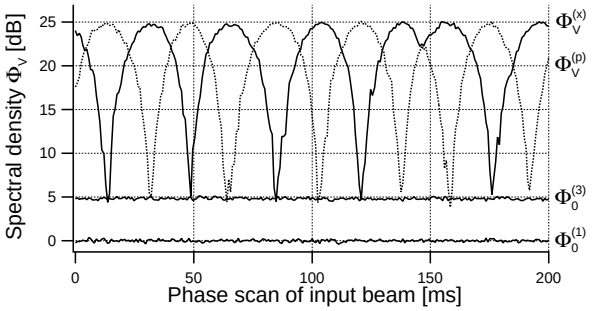

FIG. 14: Spectral density $\Phi_V(\Omega)$ relative to the vacuum level recorded by Victor while scanning the phase of the input beam. $\Phi_0^{(1)}$ is Victor's noise level for one unit of vacuum, while $\Phi_0^{(3)}$ shows the 2 extra units making 3 total units of vacuum noise measured in an attempt to recreate Alice's vacuum state input without any entanglement. $\Phi_V^{(x)}$ and $\Phi_V^{(p)}$ show the recreation of Alice's input coherent modulation amplitude of 24.9 dB, demonstrating that the peak input and output amplitudes are equal, and the x and p quadratures are indeed $\pi/2$ apart in phase. Victor's LO was phase-locked to the x and p quadratures respectively for these measurements.

of the optical carrier, and the phase of the RF signal at our measurement frequency, 1.475 MHz. We have already discussed optical phases in detail in Sec. IV A above, and indeed implicitly assumed correct optical phases in the discussion on finding optimal gain. In discussing RF phase, we will continue to assume that our optical phase-lock servos are working correctly.

Our goal is quantum noise subtraction at our analysis frequency, between the correlated beams EPR1 (measured at Alice and sent to Bob via the classical channels) and EPR2 at Bob's beamsplitter. Obviously, the best way to achieve this goal is for the relative RF phases of EPR1 and EPR2 to be zero for perfect subtraction. However, this is quite impractical in the current laboratory setup since EPR2 arrives at Bob's beamsplitter directly from the EPR beamsplitter, while EPR1 takes a very indirect route involving electrical photocurrents that travel much slower than light. It is sufficient, therefore, to ensure that the relative phase difference is a factor of 2π by implementing delays in the classical channels between Alice and Bob. In practice, we can also keep the phase difference any multiple of π and compensate for this by flipping the sign of Bob's optical phase-lock error signal. In this way, Bob *adds* EPR1 and EPR2 instead of subtracting them, thereby optically creating a π RF phase shift that compensates for the π phase delay in the classical channels.

Finally, Bob's two modulators must provide pure phase and amplitude modulation, respectively. This condition is satisfied by carefully controlling the input beam polarizations for the two temperature compensated EOMs.

Some care must be given to the maximum time delay allowed in our classical channels. This is set by the OPO linewidth (HWHM) of 5.4 MHz, corresponding to a correlation time between EPR1 and EPR2 of about 30 ns if the full bandwidth of the OPO were employed for teleportation. For a more detailed discussion see Ref. [18].

However, in our experiment, a much smaller effective bandwidth is employed corresponding to the detection bandwidth for Alice, the bandwidth of the classical channel from Alice to Bob, and the frequency range of Bob's modulators. Finally, there is the bandwidth employed by Victor in his verification of the protocol. For simplicity, here we assume that the effective detection bandwidth of our protocol is equal to the RF bandwidth, ν, of the spectrum analyzer employed by Victor in his analysis, typically around $\nu = 30$ kHz (see figures in Sec. IV C). The relevant issue is the ratio between our analysis frequency, $\Omega/(2\pi) = 1.475$ MHz, and ν. We see that this ratio is about 50 cycles. Thus 2π of RF phase delay in our classical channels contributes to a roughly 2% effect on the noise subtraction quality, which is small but not negligible.

When the gain and RF phase of the classical channels as well as the optical phases at Alice's and Bob's detectors were suitably optimized, Victor recorded a stable output while the phase of the unknown input state was being scanned, independent of the input state amplitude and phase over a wide range, as discussed below. In the case of vacuum input we obtain the flat trace at 4.8 dB (trace $\Phi_0^{(3)}$) in Fig. 14. The trace remained stable for tens of minutes, with fluctuations on the order of ± 0.1 dB.

It was not a trivial task to realize the balance of the two classical channels due to above-mentioned reasons. One practical way that we employed to optimize the system and to judge the effectiveness of the two classical channels was to send RF modulated optical fields at 1.475MHz through the two injection ports of the OPO cavity. These modulated optical signals were allowed to propagate to Alice and Bob, just as the EPR beams would in the pres-

ence of blue pump. We could then easily optimize the subtraction of the two classical fields at Bob's 99/1 beamsplitter. In terms of the conditions stated above, this *classical noise* subtraction directly mimics the *quantum noise* subtraction that we perform using the entangled EPR state during quantum teleportation, which means that if we obtain good classical subtraction, we should in fact be operating at the optimal conditions for quantum teleportation. Typically the subtraction was about 25 dB for each channel.

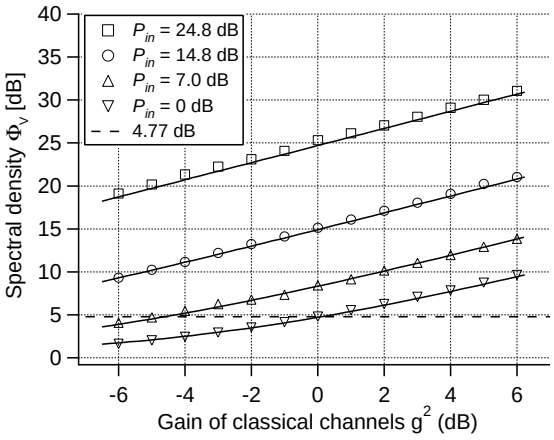

FIG. 15: Measured spectral density $\Phi_V(\Omega)$ from Victor's balanced homodyne detector as a function of gain for different amplitude-modulated coherent state and comparison with theory. The parameters for the theoretical curves were the measured visibilities: $\xi_1 = 0.985$, $\xi_2 = \xi_3 = 0.994$, $\xi_4 = 0.985$, $\xi_5 = 0.985$ and the detector quantum efficiency was $\alpha = 0.988$. The measurement frequency was 1.475 MHz. P_{in} corresponds to the actual power of the input state presented to Alice, in dB above the vacuum state.

In order to check the linearity and dynamical range for the classical channels, we measured Victor's output noise levels as a function of gain for input modulation sidebands of various amplitudes when the two classical channels were balanced. Fig. 15 shows the results for input beams with the following modulation amplitudes: 0 dB (vacuum), 7.0 dB, 14.8 dB and 24.8 dB, where in each case the full 2π of phase variation was explored. It shows that the linearity is very good from 0 dB to 25 dB input modulation amplitudes, which means we can teleport any coherent state amplitude within that range. The theoretical traces on the figure are based on our measured efficiencies without any adjustable parameters.

C. Teleportation results

Fig. 16 shows quantum teleportation results for a coherent input state. All traces are Victor's measured variances at 1.475 MHz and at pump power of 33/35 mW in the OPO paths 1 and 2, respectively. The amplitude of the input state was about 25.5dB higher than the vacuum level. Trace (a) is one unit of the vacuum noise, that is, the vacuum-state level or shot-noise level (SNL) of Victor, which is obtained by blocking Bob's beam. Trace (b) marks the 3 units of vacuum noise in the case of absent EPR beams but with Alice and Bob engaged nonetheless in the teleportation protocol, which is 4.8 dB above the SNL with our efficiencies close to 1 and is obtained by blocking the blue pumps in the experiment. Trace (c) shows the phase sensitive noise when the EPR beams and the AM sidebands on the input state are present, while Victor's LO is phase-locked to the x quadrature. Locking Victor's LO to the p quadrature produces an analogous trace with the peaks offset by $\pi/2$ in phase. Closer inspection of traces such as (c) in Fig. 16 shows that the minimum noise level is approximately 1.1 dB below the level of three units of the vacuum, although it is rather difficult to get an accurate reading because of the mismatch of scan rate and detection bandwidths. This noise level corresponds to 2.3 vacuum units. The peak of the trace should have the same amount of noise reduction, that is, from 354.8 to 354.1 vacuum units (from 25.50 dB to 25.49 dB), but this reduction is too small to observe in the graph. Trace (d) corresponds to the vacuum input state, which is obtained by blocking the modulated input beam. Acquisition parameters are: resolution bandwidth 30 kHz, video bandwidth 1 kHz and sweep time 200 ms.

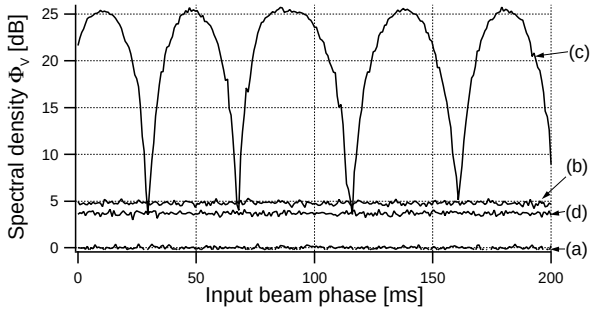

FIG. 16: Spectral density $\Phi_V(\Omega)$ recorded by Victor with the phase of the input beam scanning. Trace (a) is Victor's shot-noise level, trace (b) marks the 3 units of vacuum noise measured without entanglement, trace (c) is one quadrature of the teleported output coherent state, and trace (d) is the teleported output vacuum state (see text for details). For trace (c) Victor's LO was phase-locked to the x quadrature, while for traces (a), (b) and (d) Victor's LO was freely scanned, and a ten trace average was used. The average OPO pump power was 34 mW per beam, measurement frequency 1.475 MHz, RBW 30 kHz, and VBW 1 kHz.

The best noise reduction that we have obtained to date is shown in detail in Fig. 17. With the EPR beams present, the variances recorded by Victor are $\sigma_V^x = \sigma_V^p = 3.54 \pm 0.19$ dB, while with the EPR beams absent, $\sigma_V^x = \sigma_V^p = 4.86 \pm 0.12$ dB. The entanglement of the EPR beams thus leads to a quantum noise reduction of 1.32 ± 0.16 dB. This result was obtained with

40 mW pump power in each OPO path. The measurement parameters are the same as that in Fig. 16 except that the sweep time was 640 ms and we use a ten trace average for all traces. For this particular trace, the measured detection efficiencies were characterized by $\xi_1 = 0.986, \xi_2 = \xi_3 = 0.990, \xi_4 = 0.980, \xi_5 = 0.975$, and $\alpha_{Ax} = \alpha_{Ap} = \alpha_V = 0.988$.

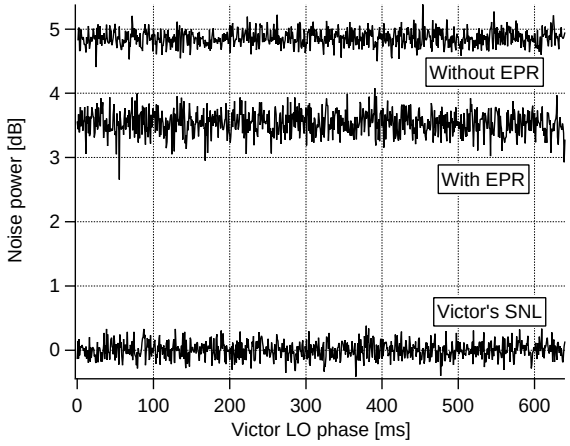

FIG. 17: Noise recorded by Victor showing in detail the reduction in the noise level with EPR beams (entanglement) present. With EPR beams, the measured variance at Victor was $\sigma_V^x = \sigma_V^p = 3.54 \pm 0.19$ dB. The average OPO pump power was 40 mW per beam, and acquisition parameters are the same as in Fig. 16. All traces use a ten trace average. SNL stands for shot-noise level.

A study of the dependence of the output variance on OPO pump power yields further insight into the experiment. Fig. 18 shows the variances of Alice and Victor as functions of pump power. From the squeezing results in Fig. 10, we can see that as the pump increases, both the squeezing and anti-squeezing increase, even though the squeezing increases very slowly. Therefore, the entanglement becomes stronger with increasing pump power. This phenomenon is reflected in the data shown in Fig. 18 at pump powers below 30 mW, where Alice's variance increases with pump power, whereas Victor's variance drops below 4.8 dB, as predicted. The best noise reduction for Victor was around 30 mW of blue pump for this particular set of data. Higher pump power did not help to reduce the noise; it instead increased both Alice's and Victor's variances even though we expect Victor's variance to continue to decrease, or at least remain stable. The likely culprits responsible for this degradation in performance will be discussed in the next sections. Chief among them is the performance of the various locking servos. As discussed in Sec. II B, fluctuations around the nominal ideal settings (e.g., $\pi/2$ for the squeezed beams that form the EPR beams) allows excess noise to contaminate the "quiet" quadratures, an effect that becomes more important as the degree of squeezing is increased.

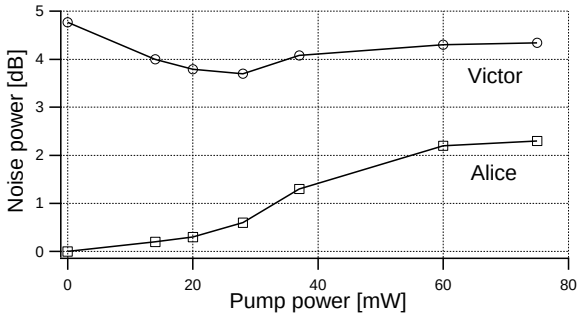

FIG. 18: Noise measured by Alice and Victor as functions of the pump of the OPO. The data points have been connected to ease viewing.

D. Teleportation fidelity

From the measured variances reported in Sec. IV C above, we can gauge the quality of the protocol by inferring the fidelity F via Eqs. (2) and (4). We first assume that the noise in the teleported output state ρ_{out} obeys Gaussian statistics [7, 9]. From the data in Fig. 17, where $\sigma_V^x = \sigma_V^p = 3.54 \pm 0.19$ dB, and where the gain g has already been set to unity by the techniques described in Sec. IV B, direct application of Eq. (2) gives $F = 0.61 \pm 0.02$.

Note that no correction whatsoever has been applied to this result; it corresponds to the fidelity obtained directly from Victor's photocurrent. We can certainly attempt to infer the fidelity associated with the field emerging from Bob's beamsplitter, rather than the photocurrent detected by Victor. To do so, we return to the issue pointed out earlier that we calibrate $g_{x,p}$ by ensuring $\beta_V = \beta_{in}$ as opposed to $\beta_{out} = \beta_{in}$. From the discussion in Sec. II A, we see that if Victor had unit detection efficiency ($\xi_5 = \eta_V = 1$), this issue would not arise at all. In our experiment where ($\xi_5 < 1, \eta_V < 1$), the actual unnormalized gains $g_{(0)}$ were set to be too large by a factor $(\xi_5\eta_V)^{-1}$ than that neccessary for optimal reconstruction of Bob's field, instead of Victor's photocurrent. We can use Eq. (4) to compare Victor's variances when ($\xi_5 = \eta_V = 1$) and when ($\xi_5 < 1, \eta_V < 1$) with the same degree of squeezing as in Fig. 17. We thus infer that if Victor had perfect detectors, the variance of Bob's teleported output field (or equivalently now, Victor's variance as measured by his photocurrent) is given by $\sigma_W^{(x,p)} = \sigma_V^{(x,p)} = 3.47$ dB above the shot-noise level, which corresponds to an inferred fidelity of $F_B = 0.62$.

Returning to fidelity referenced to Victor's photocurrent, we estimate that with 42 mW pump power in each OPO path, where we have measured -3.73 dB squeezing and 6.9 dB anti-squeezing at Victor (see Fig. 9), the EPR entanglement at the EPR beamsplitter is characterized by the factors: $\sigma^- = -3.97$ dB and $\sigma^+ = 7.0$ dB. These numbers were obtained by back-propagating the

squeezed beams to the EPR beamsplitter from Victor's homodyne detectors, considering the effects of Victor's homodyne efficiency $\xi_5 = 0.972$, photodiode quantum efficiency $\alpha_V = 0.988$ and the EPR homodyne efficiency $\xi_{EPR} = 0.985$. With measured efficiencies $\xi_1 = 0.985$, $\xi_2 = \xi_3 = 0.990$, $\xi_4 = 0.980$, $\xi_5 = 0.975$, the predicted variance of the teleported output state emerging from Bob's beamsplitter is $\sigma_W^{(x)} = \sigma_W^{(p)} = 2.82$ dB. The inferred fidelity would then be $F_P = 0.69$.

By contrast, our best entanglement-assisted noise reduction measured by Victor's balanced detector is 1.32dB below the level with no EPR beams, which corresponds to $\sigma_V^{(x)} = \sigma_V^{(p)} = 3.54$ dB and an inferred fidelity $F = 0.61$, as has been discussed.

To gain more insight into this discrepancy, we performed an analogous study to that shown in Fig. 18, where we plot the inferred fidelities from the measured variances versus pump power in Fig. 19. The inferred experimental fidelities peak at around 30mW corresponding to the minimum in Victor's measured variance. Here we also show the values of F that we might be able to reach with the current apparatus. First of all, the square symbols in Fig. 19 derive from the inferred degrees of squeezing at the EPR beamsplitter that are deduced from the data in Fig. 10. This was done from the measurement results by back-propagating the squeezed beams from Victor's homodyne detector to the EPR beamsplitter as previously described. In addition, the triangles in Fig. 19 correspond to the inferred fidelities from the theoretically predicted degrees of squeezing given by the solid line in Fig. 10. It can be seen that the disagreement between the predicted and measured fidelities is already apparent at low pump powers. However, the mismatch becomes more pronounced at higher pump powers where the measured fidelities start to decrease rather than increase with the pump level.

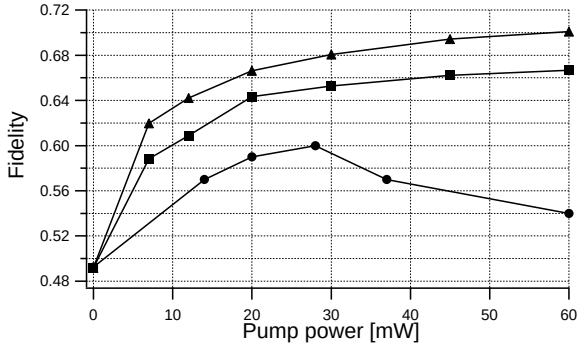

FIG. 19: Fidelity as a function of the OPO pump. Dots are the experimentally measured fidelities, squares are the expected fidelities given the measured degrees of squeezing shown in Fig. 10, and triangles are the expected fidelities based on our theoretically predicted degrees of squeezing in Fig. 10. Again, the lines connecting the data points are to ease viewing.

There are several factors contributing to the discrepancy between the measured and predicted variances and fidelities. The first is phase fluctuations from different locking systems, especially the EPR phase-lock. As discussed in Sec. II B, phase fluctuations add extra noise to the quadratures, and this effect is more pronounced at higher pump powers where the anti-squeezed quadrature is large. Another factor is the bandwidth of our two classical channels, which by bad design on our part, has been found to have excessive phase variation over the relevant RF bandwidth for the undistorted transmission of classical information. In fact, by an aforementioned technique, we measured the actual subtraction of the RF signal at 1.475 MHz through the classical channels and EPR2. It was found that frequency offsets of about 5 kHz led to drops in the cancellation from -25 dB to -20 dB. When the offset was 20 kHz, the cancellation is only -9 dB. Increasing the bandwidth while keeping relatively high isolation for the filter for various control signals (e.g., modulations at 3 and 5 MHz) in the classical channels will be helpful. A third reason for the discrepancy in Victor's variances is the imperfect character of Bob's EOMs, which cause coupling between the x and p quadratures, again resulting in contamination between squeezing and anti-squeezing. In order to reach higher fidelity, we are working to improve these aspects of the experiment.

V. CONCLUSION

We have described the details of recent experimental work to perform quantum teleportation for continuous variables. We have discussed a real experimental system where we considered many of the prevalent loss sources in our experiment, thus providing a detailed analysis of how the variances measured at Alice and Victor during teleportation vary with squeezing and ultimately OPO pump power. Phase fluctuations due to imperfect locking systems were also discussed, and it has been shown that nonideal detection schemes as well as phase fluctuations eventually degrade the noise reduction recorded by Victor and consequently reduce the teleportation fidelity.

We have discussed how to prepare experimentally the entangled EPR beams. Our entangled EPR fields at the EPR beamsplitter were typically characterized by $\sigma^- \simeq -4$ dB and $\sigma^+ \simeq 7$ dB according to our measured squeezing and efficiencies, which implies that our measured prospective fidelity would be 0.69.

The experimental setup and procedure was described in detail, including the OPO, the source of the entangled EPR fields. We have discussed optical phase-lock servo systems that ensure Alice is able to correctly measure the two orthogonal quadratures, x and p. Lastly, we have also described our classical channels through which classical information in the form of photocurrents obtained by Alice can be sent to Bob with the goals of minimal distortion and proper phase and gain in order to be sure that Bob can use that information to recover the original input state. The teleportation procedure was inves-

tigated for arbitrary unknown coherent states with any phase and a wide range of amplitudes.

The experiment clearly revealed the quduties that limit the classical performance of such a teleportation system. Victor unavoidably measures two extra units of vacuum noise if there is no entanglement. By employing the entangled fields of the EPR state, we demonstrated that the quduties were suppressed by -1.32 ± 0.16 dB, which corresponds to an inferred fidelity of $F = 0.61 \pm 0.02$ for coherent states, which when corrected for the efficiency of detection by Victor, gives a fidelity of 0.62. The apparatus was shown to succeed for arbitrary coherent states with amplitudes up to 25dB above the vacuum level. This demonstrates that with entanglement, the procedure exhibits better performance than the classical bound of fidelity $F = 0.50$ [9, 10], and hence is genuinely a quantum protocol for unconditional teleportation.

We discussed Alice's and Victor's measured variances as functions of OPO pump power. The data in Fig. 18 showed that at low pump powers, Alice's measured variance σ_A increased and Victor's measured variance σ_V decreased with pump power, as expected. However, at higher pump powers (above ≈ 30 mW), while σ_A continued to increase with pump as expected, σ_V did not continue to decrease, but began increasing instead. This implied that the anti-squeezing quadrature contaminates the squeezed quadrature at high pump powers. Possible reasons for this contamination include fluctuations in the phase-lock servos, limited classical channel bandwidth and impure amplitude and phase modulators at Bob's station.

It is encouraging to note that our high detection efficiencies together with the relatively high degree of entanglement that we have achieved shows that our apparatus is capable of producing higher fidelity between the input and output states. In addition, a new scheme with the OPO pumped only by a single unidirectional blue beam to form the EPR state is being planned. We could then hope to obtain over -5 dB of entanglement by mitigating high BLIIRA, and thus reducing the intracavity losses in the OPO. Such capabilities would be of interest to quantum information processing with continuous quantum variables [26].

Acknowledgments

The contributions of J. Buck and A. Furusawa are gratefully acknowledged. This research was funded by the National Science Foundation, by the Office of Naval Research, by the Caltech MURI on Quantum Networks administered by the Office of Army Research, and by the NSF sponsored Institute for Quantum Information. TCZ was partially supported by the EYTP of MOE, P. R. C.

[1] W. K. Wootters and W. H. Zurek, Nature **299**, 802 (1982).
[2] C. H. Bennett, G. Brassard, C. Crepeau, R. Jozsa, A. Peres, and W. K. Wootters, Phys. Rev. Lett. **70**, 1895 (1993).
[3] J. Preskill, *Lecture notes for Physics/Computer Science 219: Quantum Computation*, http://www.theory.caltech.edu/people/preskill/ph229 (1998).
[4] M. A. Nielsen and I. L. Chuang, *Quantum Computation and Quantum Information*, (Cambridge Univ. Press, Cambridge, 2000).
[5] D. Bouwmeester, J.-W. Pan, K. Mattle, M. Eibl, H. Weinfurter, and A. Zeilinger, Nature **390**, 575 (1997).
[6] D. Boschi, S. Branca, F. De Martini, L. Hardy, and S. Popescu, Phys. Rev. Lett. **80**, 1121 (1998).
[7] A. Furusawa, J. L. Sørensen, S. L. Braunstein, C. A. Fuchs, H. J. Kimble, and E. S. Polzik, Science **282**, 706 (1998).
[8] M. A. Nielsen, E. Knill, and R. Laflamme, Nature **396**, 52 (1998).
[9] S. L. Braunstein, C. A. Fuchs, and H. J. Kimble, J. Mod. Opt. **47**, 267 (2000).
[10] S. L. Braunstein, C. A. Fuchs, H. J. Kimble, and P. van Loock, Phys. Rev. A **64**, 022321 (2001).
[11] Recent press reports have described continuous variable teleportation from the group of H. Bachor and P. K. Lam at the Australian National University. Unfortunately, there is no scientific manuscript on which to base an assessment of these claims.
[12] J. L. Sørensen, "Nonclassical light for atomic physics and quantum teleportation", Ph.D. thesis, University of Aarhus (1998).
[13] The measurements described here were first reported at the 2001 Annual Meeting of the Optical Society of America, paper WG5 entitled "Quantum teleportation of quadrature phase amplitudes".
[14] S. L. Braunstein and H. J. Kimble, Phys. Rev. Lett. **80**, 869 (1998).
[15] L. Vaidman, Phys. Rev. A **49**, 1473 (1994).
[16] A. Einstein, B. Podolsky and N. Rosen, Phys. Rev. **47**, 777 (1935).
[17] S. J. van Enk, Phys. Rev. A **60**, 5095 (1999).
[18] P. van Loock, S. L. Braunstein, and H. J. Kimble, Phys. Rev. A **62**, 022309 (2000).
[19] E. S. Polzik, J. Carri, and H. J. Kimble, Phys. Rev. Lett. **68**, 3020 (1992); Appl. Phys. B **55**, 279 (1992).
[20] E. S. Polzik and H. J. Kimble, Opt. Lett. **16**, 1400 (1991).
[21] H. Mabuchi, E. S. Polzik, and H. J. Kimble, J. Opt. Soc. Am. B **11**, 2023 (1994).
[22] L. Shiv, J. L. Sørensen, E. S. Polzik, and G. Mizell, Opt. Lett. **20**, 2270 (1995).
[23] Z. Y. Ou, S. F. Pereira, and H. J. Kimble, Appl. Phys. B **55**, 265 (1992).
[24] Z. Y. Ou, S. F. Pereira, H. J. Kimble, and K. C. Peng, Phys. Rev. Lett. **68**, 3663 (1992).
[25] S. J. van Enk, J. of Mod. Opt. **48**, 2049 (2001).
[26] S. L. Braunstein and A. K. Pati (eds.), *Quantum Information Theory with Continuous Variables*, (Kluwer Aca-

demic Publishers, Dodrecht, 2000, in press).